Near-field infrared spectroscopy of monolayer $MnPS_3$

Sabine N. Neal,[1] Heung-Sik Kim,[2] Kevin A. Smith,[1] Amanda V. Haglund,[3] David G. Mandrus,[3] Hans A. Bechtel,[4] G. Lawrence Carr,[5] Kristjan Haule,[2] David Vanderbilt,[2] and Janice L. Musfeldt[1,6]

[1]*Department of Chemistry, University of Tennessee, Knoxville, Tennessee 37996, USA*
[2]*Department of Physics and Astronomy, Rutgers University, Piscataway, New Jersey 08854, USA*
[3]*Department of Materials Science and Engineering, University of Tennessee, Knoxville, Tennessee 37996, USA*
[4]*Advanced Light Source Division, Lawrence Berkeley National Laboratory, Berkeley, California 94720, USA*
[5]*National Synchrotron Light Source II, Brookhaven National Laboratory, Upton, New York 11973, USA*
[6]*Department of Physics and Astronomy, University of Tennessee, Knoxville, Tennessee 37996, USA*

(Received 28 June 2019; revised manuscript received 19 July 2019; published 22 August 2019)

We measured the near-field infrared response of $MnPS_3$ in bulk, few-, and single-layer form and compared our findings with traditional far-field vibrational spectroscopies, a symmetry analysis, and first-principles lattice dynamics calculations. Trends in the B_u mode near 450 cm^{-1} are striking, with the disappearance of this structure in the thinnest sheets. Combined with the amplified response of the activated A_g mode and analysis of the $A_u + B_u$ features, we find that symmetry is unexpectedly increased in few- and single-sheet $MnPS_3$ due to a restoration of the threefold axes of rotation. Monoclinicity in this system is therefore a consequence of the long-range stacking pattern and temperature rather than local structure.

DOI: 10.1103/PhysRevB.100.075428

I. INTRODUCTION

The layered structures of many chalcogenides allow for exfoliation, providing a unique platform for combining the complexity of bulk materials with the tunability of few- and single-layer systems [1]. One of the most widely investigated van der Waals solids is MoS_2 [2–5]. Major findings include the indirect → direct gap crossover at the single layer level [3,4], valley splitting driven by spin-orbit coupling [6,7], and confinement and symmetry-breaking effects that lead to unique chemical, electronic, and thermal properties [8–11]. Complex chalcogenides are also attracting attention [8,12]. One interesting initiative involves the creation of robust, single-layer magnetic semiconductors like CrI_3, $CrSiTe_3$, and $MnPS_3$ [13–16]. A commonality between all of these systems—from MoS_2 to $MnPS_3$—is the role of Raman scattering to assure sample quality, probe even-symmetry vibrational modes, and uncover single-layer properties [5,17–19]. Odd-symmetry modes are, however, completely unexplored in few-layer materials. Infrared spectroscopy is well suited for examining the fundamental excitations of the lattice, and because the technique probes odd-symmetry vibrations, it is useful for revealing ferroelectric, vibronic, and spin-lattice coupling mechanisms [20–23]. Although it is highly desirable to extend toward few- and single-layer chalcogenides, traditional infrared spectroscopy cannot beat the diffraction limit for small sized (exfoliated) flakes [24,25]. In other words, long wavelength far infrared light cannot be focused tightly enough to measure high-quality sheets.

Synchrotron-based infrared nanospectroscopy offers a path forward. This technique combines a high brightness, broadband synchrotron light source [26] with Fourier transform techniques and a tip-enhanced approach to enable spectroscopic work on small-sized samples and materials with micro- and nanoscale texture [24,25,27–29]. The spatial resolution, achieved by focusing infrared light onto an atomic force microscope (AFM) tip [Fig. 1(c)], is on the order of 20 × 20 nm^2. The distinct advantage of tip-enhanced work is that spectra can be collected from samples that were previously out of reach. Initially, this technique was confined to the middle infrared [24,25] and proved powerful for exploring polaritons in graphene, unveiling the inhomogeneous character of the phase transition in VO_2, and studying heterogeneity in Bi_2Se_3 and Sb_2Se_3 nanocrystals [30–33]. Recently, the operational window has been extended into the far infrared—down to 330 cm^{-1} [27]. Near-field infrared spectroscopy is therefore inviting new approaches to studying chalcogenides. This is because many (but not all) of the characteristic vibrational modes of these materials resonate in this frequency window. What distinguishes synchrotron-based near-field spectroscopy from tip-enhanced Raman scattering is the ability to explore odd- (rather than even-) symmetry vibration modes [34]—although occasionally features are activated for various reasons as discussed elsewhere in the text.

We selected $MnPS_3$ as a platform with which to examine these ideas. This compound belongs to a large family of metal phosphorus trichalcogenides with the formula MPX_3 where M = metal ion, in this case high spin Mn^{2+} ($S = \frac{5}{2}$), and X = chalcogen. This system is considered to be a collinear antiferromagnet below $T_N = 78$ K [36] because it can be described by a Heisenberg spin Hamiltonian on a honeycomb lattice. It has also been reported to be ferrotoroidic [37], suggesting that there may be weak noncollinearity that has not yet been explored. MPX_3 compounds can be viewed as salts of the thiophosphate anion, with Mn^{2+} cations and $(P_2S_6)^{4-}$ anions. These cations are linked together by Mn-X bonds, which are weaker than the bonds in the anion unit. This allows for a conceptual division of vibrational features into internal

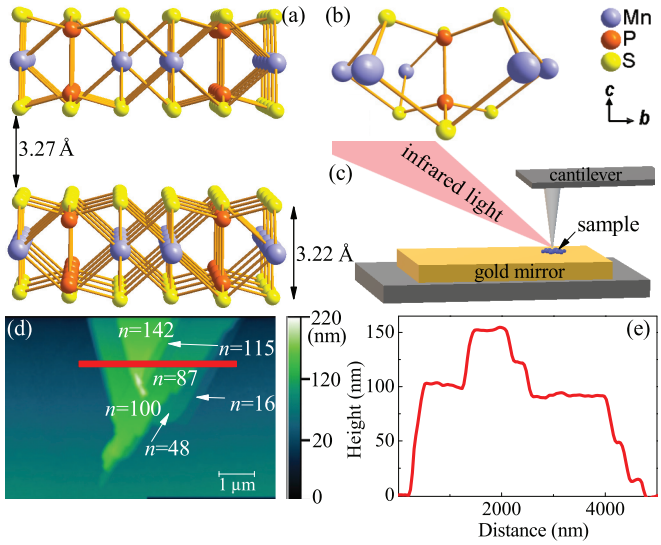

FIG. 1. (a) Crystal structure of monoclinic $MnPS_3$ showing the slab thickness and interlayer distance. (b) Local structure for monolayer $MnPS_3$ emphasizing the bonding around the Mn center and the P-P dimer [35]. (c) Close-up schematic of the near-field setup showing the cantilever tip directing light to focus on a small area of the sample. Spatial resolution is on the order of 20×20 nm^2. (d) High resolution AFM image along with the corresponding layer number, extracted from (e) the height profile along the red line in (d).

modes of the anion and external modes from the interactions between cation and anion [38]. Figure 1(a) shows the stacking of $MnPS_3$, which is characteristic of a monoclinic van der Waals solid [35]. The individual layer thickness is ≈3.22 Å. Each slab is separated by a ≈3.27 Å van der Waals gap. The local structure [Fig. 1(b)] is especially sensitive to symmetry. Rather than $C2/m$ like the bulk, the monolayer is proposed to be $P\bar{3}1m$—assuming that the internal structure remains intact [39]. At this time, the presence of a higher symmetry space group in the monolayer is experimentally untested and is one of the goals of this work. Extensive investigation of Raman scattering and light emission in $MnPS_3$ and related systems reveals strong electron-phonon coupling of the even-symmetry modes as well as field-effect transistor behavior [17,40–43]. Because trends in the odd-symmetry (ungerade) vibrational modes are crucial for uncovering local structure modifications, testing various parent and subgroup candidates, and developing higher-level functionalities like ferroelectricity [20,44–46], bringing infrared spectroscopy to the field of few- and single-layer chalcogenides is an important step forward.

In order to explore the odd-symmetry vibrational properties of few- and single-layer chalcogenides, we measured the near-field infrared response of $MnPS_3$ and compared our findings to traditional infrared absorption and Raman scattering spectroscopy, complementary lattice dynamics calculations, and a symmetry analysis. We find that features in the near-field spectrum of the single crystal are a combination of both infrared- and Raman-active modes. This mixed activation is a consequence of the tip-based nature of the technique which significantly enhances the electric field. Detailed analysis of the near-field spectra supports a thickness-induced symmetry crossover. The behavior of the B_u mode is most revealing in this regard. It disappears in the thinnest sheets, indicative of a symmetry increase. We analyzed a number of different candidate space groups in order to uncover the symmetry relationship and find that $C2/m \leftrightarrow P\bar{3}1m$ is most consistent with our data. We propose that the restoration of the threefold rotation in few- and single-layer $MnPS_3$ is induced by a combination of long-range stacking modifications and temperature effects. This is significant because local and long-range symmetry determine functionality in a variety of materials.

II. METHODS

High quality single crystals of $MnPS_3$ were prepared via chemical vapor transport as described previously [47]. Surface-exfoliated crystals were mounted on pin-hole apertures for both infrared and Raman measurements. Traditional far-field infrared studies were performed on a Bruker IFS 113v Fourier-infrared spectrometer equipped with a bolometer detector over the 20–700 cm^{-1} frequency range with 2 cm^{-1} resolution. The measured transmittance was converted to absorption as $\alpha(\omega) = -\frac{1}{d}\ln[\mathcal{T}(\omega)]$, where $\mathcal{T}(\omega)$ is measured transmittance and d is the thickness. No attempt was made to carry out a reflectance correction to the transmittance. Raman scattering was performed on a LabRAM HR Evolution Raman spectrometer (50–700 cm^{-1}) using an excitation wavelength of 532 nm at a power of 0.5 mW with an 1800 line/mm grating.

Synchrotron-based infrared nanospectroscopy was performed using a commercial nanoscope (neaSNOM, Neaspec GmbH) using the setup at beamline 2.4 at the Advanced Light Source at Lawrence Berkeley National Laboratory [24]. Both amplitude and phase data were collected over the 330–700 cm^{-1} range. A Ge:Cu detector equipped with 2 MHz, low-noise preamplifier, a KRS-5 beamsplitter, and a nitrogen enclosure enabled extension to the far infrared. A detailed discussion of the typical single-to-noise ratio is provided in the Supplemental Material [48].

Prior to the near-field work, single crystals were mechanically exfoliated with thermal release tape and applied to a substrate. The exfoliated flakes are extremely small in size (between a micron and a few nanometers) and have almost no optical density. A tip-enhanced technique is therefore required in order to obtain the necessary spatial resolution for a measurement and to reveal the symmetry evolution of the phonons of few- and single-sheet $MnPS_3$. As discussed in the text, we tested a number of candidate substrates before selecting an uncoated gold mirror. The sample + substrate are scanned with atomic force microscopy (AFM), first taking a low resolution image to locate possible regions of interest. Once a promising area is confirmed, a high resolution AFM image is used to reveal the full topography. This information is used to (i) confirm cleanliness, (ii) extract a height profile, and (iii) designate areas to measure. Since AFM and near-field infrared operate in the same field of view, we can pinpoint exactly where to collect spectra. Repeated measurements over several hours confirmed that the sheets are stable. Sheet thickness was calculated using $xm + yn = H$, where H is the extracted height (nm), x is the sheet thickness (nm), y is the van der Waal gap thickness, m is the number of sheets, and n is the number of van der Waal layers present which is defined

as $n = (m - 1)$. Specifically for $MnPS_3$ $x = 0.322$ nm and $y = 0.327$ nm. The height profile (H) was extracted using the open source software Gwyddion, and we employed a standard to check our height calibration.

Ab initio density functional theory (DFT) calculations were performed employing Vienna *ab initio* simulation package (VASP), which employs the projector-augmented wave (PAW) basis set [49,50]. 340 eV of plane-wave energy cutoff and $8 \times 6 \times 8$ $(15 \times 15 \times 1)$ Monkhorst-Pack k-grid sampling were employed for monoclinic $C2/m$ (single-layer hexagonal $P\bar{3}1m$) crystal structures. For the single-layer calculation in monoclinic symmetry, a $8 \times 6 \times 1$ k grid was employed along with the bulk in-plane lattice parameters a and b. For the treatment of electron correlations within DFT, a revised Perdew-Burke-Ernzerhof exchange-correlation functional for crystalline solid (PBEsol) was employed [51], in addition augmented by on-site Coulomb interactions for transition metal d orbitals within a simplified rotationally invariant form of DFT + U_{eff} formalism [52]. Structural optimizations employed force criteria below 10^{-4} eV/Å. PHONOPY code interfaced with VASP was employed to calculate the Γ-point phonon modes for each structure [53].

III. RESULTS AND DISCUSSION

A. Far- vs near-field infrared spectroscopy and mode assignments

Figure 2 summarizes the vibrational properties of single crystalline $MnPS_3$ at room temperature. In addition to the traditional infrared absorption, Raman scattering, and theoretically predicted mode positions, it also displays our near-field results. Combining the first-principles lattice dynamics calculations with prior literature results [54], we can assign all of the peaks in these spectra. Focusing first on the conventional infrared and Raman response, we assign the strong infrared band at 573 cm^{-1} to the nearly degenerate PS_3 stretching mode. The presence of two weak Raman bands at 569 and 581 cm^{-1} demonstrates that coupling between two PS_3 units is weak. The small infrared-active B_u mode at 452 cm^{-1} is a combination of a P-P stretch + out-of-plane PS_3 translation. The strong Raman band near 385 cm^{-1} is due to a symmetric stretch of PS_3, largely ascribed to the motion of chalcogen atoms with a weak contribution from vibrational coupling between the phosphorus and sulfur units [54]. As expected, the Mn-containing modes appear at lower frequencies. They are not included here in order to focus on the near-field frequency window that is currently available [27]. The full spectral response of $MnPS_3$ is given in the Supplemental Material [48], and our mode assignments are summarized in Table I.

Figure 2(c) displays the near-field spectrum of single crystalline $MnPS_3$—both amplitude and phase—prior to exfoliation. Assignments are made by comparison with the aforementioned traditional infrared and Raman spectroscopies as well as our calculated frequencies and displacement patterns [Figs. 2(a) and 2(b)]. Clearly the infrared-active modes are well represented in terms of position, shape, and amplitude—confirming the effectiveness of the near-field technique. For instance, the $A_u + B_u$ modes are centered near 573 cm^{-1}.

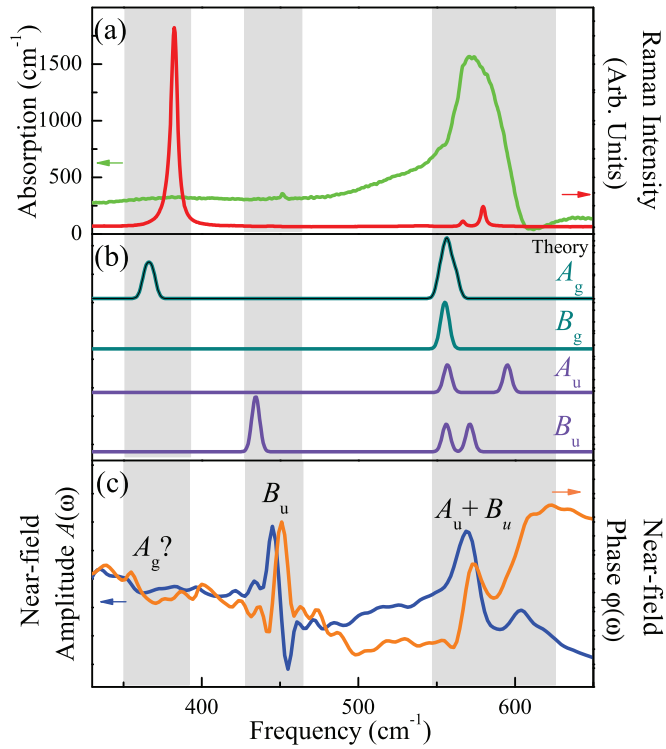

FIG. 2. (a) Traditional infrared absorption (green) and Raman scattering (red) spectra at 300 K. (b) Lattice dynamics calculations of $MnPS_3$ projected according to mode symmetry. Recall that the *ungerade* modes are infrared active, and the *gerade* symmetry modes are Raman active. The calculated frequencies are within 3% of the experimental peak positions. The calculated modes are shown with a Gaussian line shape and 2 cm^{-1} broadening. The higher peak intensity indicates near degeneracy. (c) Room temperature near-field amplitude (blue) and phase (orange) spectra for single crystalline $MnPS_3$. We set the overall frequency scale to focus on the available near-field energy window.

The much smaller B_u mode evident as well; it increases in intensity in the near-field response and is well isolated from the other features. At the same time, there is a subtle hint of an additional feature near 360 cm^{-1} that is not anticipated according to traditional selection rules. We tentatively assign it as an activated A_g mode—normally present in the Raman response. We attribute the relaxation of selection rules in the near-field spectrum of $MnPS_3$ to the fact that the electric field lines are highly concentrated and slightly curved due to

TABLE I. Vibrational mode assignments of single crystalline $MnPS_3$. All values are in cm^{-1}.

ω (infrared)	ω (Raman)	ω (near-field)[a]	Assignment
–	385	360	$\nu(PS_3)$[b]
452	–	450	$T_z'(PS_3)$[c] + ν(P-P)
573	–	567	$\nu(PS_3)$
–	569, 581	–	$\nu(PS_3)$

[a]Corresponds to maxima in the phase spectra.
[b]ν = symmetric stretch.
[c]T_z' = translational motion.

the manner in which the evanescent wave travels down the antennalike tip to focus light onto the sample [24,25,55]. Tip-enhanced techniques also have penetration depth differences compared to traditional spectroscopies [24,25,55] which may further impact the selection rules. In any case, the assignments summarized in Table I place the near-field infrared response of $MnPS_3$ on a firm foundation from which we can extend toward few- and single-layer systems.

B. Testing different substrates

As part of the work to measure atomically thin $MnPS_3$, we tested a variety of substrates for suitability with our target material. These included gold, aluminum, glass, sapphire, and silicon. The choice turns out to be crucial. Our work with uncoated gold mirrors revealed excellent adhesion of few- and single-sheet $MnPS_3$ via gold$\cdots$sulfur interactions. This not only eliminates the need for glue but also the interference of substrate phonons. The use of bare gold mirrors to support exfoliated chalcogenides does, however, have the disadvantage of introducing a small charge transfer band between the sulfur and the gold centered at 550 cm^{-1} [56]. This charge transfer excitation is somewhat problematic for $MnPS_3$ because it partially obscures some of the sulfur-related stretching modes between 550 and 600 cm^{-1}. We anticipate that uncoated gold will, however, work well for some of the heavier chalcogenides like $MoTe_2$ where the frequencies are shifted downward due to heavier masses [57]. In any case, the charge transfer band is apparent only in the single-layer response for $MnPS_3$. This feature is easily identified in the near-field response by the increasing background, the width of the band (which indicates its electronic origin), and the fact that prior studies of other sulfur-containing molecules and materials on gold display a Au$\cdots$S charge transfer band in this vicinity all point toward such an assignment [56]. We attempted to uncover the hidden $A_u + B_u$ phonons by modeling this Au$\cdots$S charge transfer with a series of Voigt oscillators and subtracting the result from the near-field spectrum. This procedure did not, unfortunately, reveal the superimposed phonons—probably due to their minute oscillator strength. This limits the frequency window for single-layer $MnPS_3$—although the response for the bilayer and above is relatively unaffected.

C. Vibrational properties of $MnPS_3$ as a function of sheet thickness

Turning our attention back to the magnetic chalcogenide, Fig. 3 summarizes the near-field infrared response of $MnPS_3$ as a function of layer thicknesses. The measured spectra of the bulk crystal and monolayer in Fig. 3(a) reveal a stunning dissimilarity, and the theoretically predicted phonon patterns capture these effects nicely—particularly with respect to the presence (or absence) of the B_u mode. Figures 3(b) and 3(c) displays a systematic view of the near-field spectrum of $MnPS_3$ as a function of layer number (n). These data and the findings from our correlation group analysis are discussed below. Taken together, they support the overall connection between decreasing layer number and a crossover to higher symmetry. The gold$\cdots$sulfur interaction is apparent in the single layer ($n = 1$) spectrum as evidenced by the charge transfer band above 550 cm^{-1} [56].

Detailed analysis of the near-field spectra [Figs. 3(b) and 3(c)] supports an n-dependent symmetry crossover. The behavior of the B_u feature at 450 cm^{-1} is most revealing. Because this mode is well isolated, its behavior can be easily tracked. This structure is very evident in the bulk ($n = \infty$), blueshifts at intermediate sheet thicknesses, diminishes between $n = 30$ and 16, and disappears entirely below $n = 11$. It never reappears—even in the monolayer—indicating that the symmetry for $n < 11$ is no longer $C2/m$. Furthermore, the symmetry must be higher, not lower, for this feature to disappear. To understand why the 450 cm^{-1} peak disappears, we calculated the phonon frequencies for two separate single-layer structures with monoclinic and hexagonal symmetry constraints [Fig. 3(d)]. We find that the modes around 450 cm^{-1} which exist in the monoclinic ($C2/m$) symmetry are absent in the hexagonal ($P\bar{3}1m$) case, indicating that the disappearance of this feature is indeed linked to the restoration of threefold symmetry in the single-layer limit.

The A_g vibrational mode near 360 cm^{-1} provides additional evidence for a change in symmetry. This feature is at the limit of our sensitivity in the bulk, becomes somewhat more apparent in the intermediate thickness range, and is fairly clear in the $n = 11$ spectrum. In few-layer systems, the trends in the A_g mode (now actually A_{1g} symmetry [58]) are less obvious, although the structure appears to be amplified in the monolayer spectrum.

The $A_u + B_u$ sulfur-phosphorous stretching modes near 556 cm^{-1} also display signatures of a thickness-dependent symmetry transition. These features are strong and relatively broad in the bulk—as expected when a number of closely related modes overlap. The B_u component of this "mode cluster" near 600 cm^{-1} is unfortunately not well isolated, therefore making it more difficult to study as compared to the 450 cm^{-1} B_u phonon. That being said, the structure evolves with decreasing thickness, always sporting a clear doublet between $n = 142$ and 48. The low frequency branch of the doublet redshifts with decreasing thickness, whereas the high frequency branch blueshifts slightly. The doublet broadens significantly between $n = 48$ and 22. Between $n = 16$ and 11, the two branches come together slightly and begin to diminish. Below $n = 11$, the features widen significantly and are much more diffuse—though never completely disappearing. Eventually (when $n = 1$), they are overcome by the gold$\cdots$sulfur charge transfer band above 550 cm^{-1} and therefore cannot be resolved [56].

D. Analyzing the symmetry crossover

In order to uncover the symmetry relationship between the single crystal and monolayer, we analyzed a number of different candidate space groups including $P\bar{3}m1$, $R\bar{3}m$, and $P\bar{3}1m$. We find that $P\bar{3}1m$ provides the best overall agreement. The symmetry relationship between $C2/m$ and $P\bar{3}1m$ is summarized in Fig 3(d). Analysis reveals that $P\bar{3}1m$ has a threefold axes that $C2/m$ does not. The inversion center is present in both settings. Importantly, $P\bar{3}1m$ (and the other candidate space groups) have higher symmetry than $C2/m$, so they will have fewer modes. This is because $C2/m$ is a maximal subgroup of $P\bar{3}m1$. After restoration of the threefold rotation, the magnetic point group becomes $3m$. The vibrational response

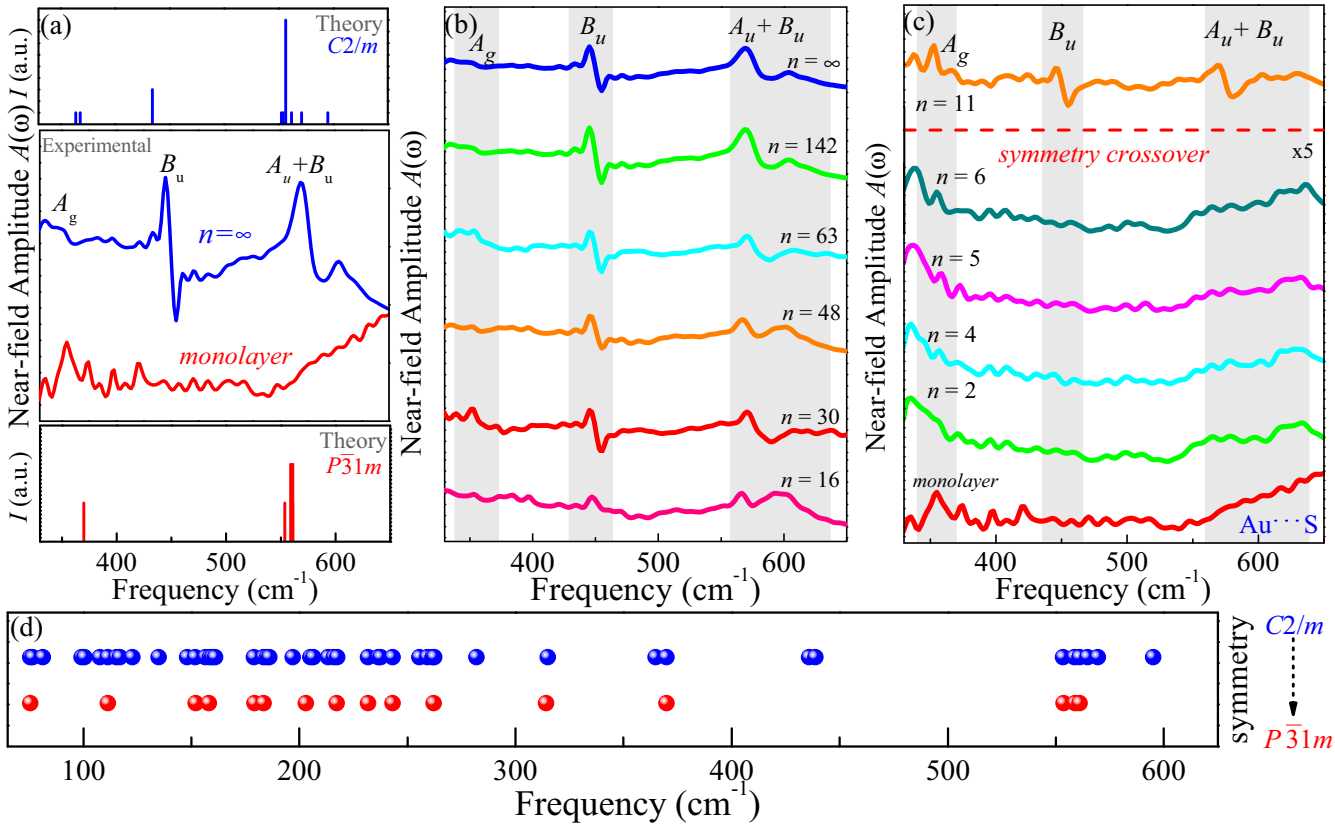

FIG. 3. (a) Near-field infrared response of $MnPS_3$ single crystal compared with that of the monolayer. The latter is multiplied by a factor of 5. Corresponding lattice dynamics calculations highlight the symmetry modifications. We show both the infrared- and Raman-active modes. (b) and (c) Evolution of the near-field infrared spectra from $MnPS_3$ single crystal ($n = \infty$) to the monolayer. The exfoliated sheets are on a gold substrate. A detailed discussion of signal-to-noise considerations is available in the Supplemental Material [48]. In (b) and (c) the spectra are shifted (by a constant amount) for clarity, the data below $n = 11$ are multiplies by a factor of 5, and the well-known Au···S signature is indicated [56]. (d) Direct comparison of the predicted vibrational modes over the entire frequency range for a single sheet of $MnPS_3$—depending on the symmetry that was imposed during the calculation ($C2/m$ vs $P\bar{3}1m$).

therefore demonstrates that the single crystal of $MnPS_3$ has lower symmetry than its few- and single-sheet analogs.

It is curious that threefold symmetry is restored below $n = 11$ rather than at $n = 1$ where the stacking becomes irrelevant. We speculate that, since interactions between adjacent layers in this wide-gap (≈2.65 eV) semiconductor are weak [59], thermal excitations may restore the higher symmetry below a critical thickness—especially at room temperature. Additional questions relate to stabilizing crystal structures with different stacking symmetries for distinct physical properties in these layered systems as a function of layer thickness or alternate growth conditions. Based on the weakness of the van der Waals interactions, it is plausible to assume the presence of alternative metastable layer stacking patterns with different symmetries as suggested in other layered van der Waals compounds [59–61]. As proposed in this work, their relative stabilities may be affected by temperature, finite-size effects, or growth conditions. This is important because certain stacking patterns may give rise to distinct magnetic order or even complex order parameters such as ferrotoroidicity [37]. In this regard, synchrotron-based near-field spectroscopy will be a crucial tool for exploring symmetry in few-layer van der Waals compounds and ultrathin oxide heterostructures.

IV. SUMMARY AND OUTLOOK

Synchrotron-based near-field infrared spectroscopy provides a unique platform for evaluating complex chalcogenides like $MnPS_3$. This technique is a fusion of a high brightness source, Fourier transform techniques, and a tip to localize and direct the radiation which enables measurement of high-quality (exfoliated) flakes. To complement this revolutionary spectroscopic approach, we also developed a general method for stabilizing complex chalcogenides in few- and single-sheet form onto a bare gold substrate. This method is outlined here and utilized to reveal the dynamics of our target material $MnPS_3$ in few- and single-layer form. Traditional infrared absorption and Raman scattering as well as complementary first-principles lattice dynamics calculations support this effort. Near-field measurements reveal dramatic changes in spectral characteristics with decreasing layer number. Perhaps the most striking trend involves the B_u mode near 450 cm^{-1} which disappears in the thinnest sheets. Combined with the amplified response of the A_g mode and analysis of the $A_u + B_u$ features, we find that symmetry is unexpectedly increased, rather than decreased, in few- and single-layer $MnPS_3$. The monoclinicity of this system is thus a consequence of the long-range stacking pattern rather than local structure. One test

of this mechanism is how the symmetry crossover manifests across the $MnPS_3$, $NiPS_3$, and $FePS_3$ series—a subject of future work. The overall significance of this effort lies in the application of synchrotron-based infrared nanospectroscopy to few- and single-sheet chalcogenides to reveal the odd-symmetry vibrational modes while, at the same time, demonstrating the potential of this approach to unlock a much wider field of investigation into the properties of atomically thin materials.

ACKNOWLEDGMENTS

Research at the University of Tennessee (J.L.M.) is supported by the U.S. Department of Energy, Office of Basic Energy Sciences, Materials Science Division under award DE-FG02-01ER45885. Work at Rutgers University is funded by the National Science Foundation DMREF Grant DMR-1629059. D.G.M. acknowledges support from the Gordon and Betty Moore Foundations EPiQS Initiative through Grant GBMF4416. A.V.H. acknowledges the support of the Center for Materials Processing, a Tennessee Higher Education Commission (THEC) supported Accomplished Center of Excellence, for funding the crystal synthesis work that provided materials for this research. Portions of these measurements utilized beamline 2.4 at the Advanced Light Source, which is a DOE Office of Science User Facility operated under Contract No. DE-AC02-05CH11231, including the remote user program from NSLS-II under contract DE-SC0012704.

[1] A. B. Kaul, J. Mater. Res. **29**, 348 (2014).
[2] X. Li and H. Zhu, Journal of Materiomics **1**, 33 (2015).
[3] K. F. Mak, C. Lee, J. Hone, J. Shan, and T. F. Heinz, Phys. Rev. Lett. **105**, 136805 (2010).
[4] A. Splendiani, L. Sun, Y. Zhang, T. Li, J. Kim, C. Y. Chim, G. Galli, and F. Wang, Nano Lett. **10**, 1271 (2010).
[5] H. Li, Q. Zhang, C. C. R. Yap, B. K. Tay, T. H. T. Edwin, A. Olivier, and D. Baillargeat, Adv. Funct. Mater. **22**, 1385 (2012).
[6] D. Xiao, G. B. Liu, W. Feng, X. Xu, and W. Yao, Phys. Rev. Lett. **108**, 196802 (2012).
[7] A. M. Jones, H. Yu, N. J. Ghimire, S. Wu, G. Aivazian, J. S. Ross, B. Zhao, J. Yan, D. G. Mandrus, D. Xiao, W. Yao, and X. Xu, Nat. Nanotechnol. **8**, 634 (2013).
[8] S. Das, J. A. Robinson, M. Dubey, H. Terrones, and M. Terrones, Annu. Rev. Mater. Res. **45**, 1 (2015).
[9] A. K. Geim and A. H. MacDonald, Phys. Today **60**(8), 35 (2007).
[10] G. R. Bhimanapati, Z. Lin, V. Meunier, Y. Jung, J. Cha, S. Das, D. Xiao, Y. Son, M. S. Strano, V. R. Cooper, L. Liang, S. G. Louie, E. Ringe, W. Zhou, S. S. Kim, R. R. Naik, B. G. Sumpter, H. Terrones, F. Xia, Y. Wang, J. Zhu, D. Akinwande, N. Alem, J. A. Schuller, R. E. Schaak, M. Terrones, and J. A. Robinson, ACS Nano **9**, 11509 (2015).
[11] L. Song, L. Ci, H. Lu, P. B. Sorokin, C. Jin, J. Ni, A. G. Kvashnin, D. G. Kvashnin, J. Lou, B. I. Yakobson, and P. M. Ajayan, Nano Lett. **10**, 3209 (2010).
[12] W. Zheng, T. Xie, Y. Zhou, Y. L. Chen, W. Jiang, S. Zhao, J. Wu, Y. Jing, Y. Wu, G. Chen, Y. Guo, J. Yin, S. Huang, H. Q. Xu, Z. Liu, and H. Peng, Nat. Commun. **6**, 6972 (2015).
[13] Y. Liu and C. Petrovic, Phys. Rev. B **97**, 014420 (2018).
[14] S. Kang, S. Kang, and J. Yu, J. Electron. Mater. **48**, 1441 (2019).
[15] M. W. Lin, H. L. Zhuang, J. Yan, T. Z. Ward, A. A. Puretzky, C. M. Rouleau, Z. Gai, L. Liang, V. Meunier, B. G. Sumpter, P. Ganesh, P. R. Kent, D. B. Geohegan, D. G. Mandrus, and K. Xiao, J. Mater. Chem. C **4**, 315 (2016).
[16] S. Lee, K. Y. Choi, S. Lee, B. H. Park, and J. G. Park, APL Mater. **4**, 086108 (2016).
[17] G. Long, T. Zhang, X. Cai, J. Hu, C. W. Cho, S. Xu, J. Shen, Z. Wu, T. Han, J. Lin, J. Wang, Y. Cai, R. Lortz, Z. Mao, and N. Wang, ACS Nano **11**, 11330 (2017).
[18] J. Lee, T. Y. Ko, J. H. Kim, H. Bark, B. Kang, S. G. Jung, T. Park, Z. Lee, S. Ryu, and C. Lee, ACS Nano **11**, 10935 (2017).
[19] Y.-J. Sun, Q.-H. Tan, X.-L. Liu, Y.-F. Gao, and J. Zhang, J. Phys. Chem. Lett. **10**, 3087 (2019).
[20] P. Chen, X. Xu, C. Koenigsmann, A. C. Santulli, S. S. Wong, and J. L. Musfeldt, Nano Lett. **10**, 4526 (2010).
[21] K. R. O'Neal, J. M. Patete, P. Chen, B. S. Holinsworth, J. M. Smith, N. Lee, S. W. Cheong, S. S. Wong, C. Marques, M. C. Aronson, and J. L. Musfeldt, J. Chem. Phys. **141**, 044710 (2014).
[22] J. Deisenhofer, I. Leonov, M. V. Eremin, C. Kant, P. Ghigna, F. Mayr, V. V. Iglamov, V. I. Anisimov, and D. van der Marel, Phys. Rev. Lett. **101**, 157406 (2008).
[23] L. D. Casto, A. J. Clune, M. O. Yokosuk, J. L. Musfeldt, T. J. Williams, H. L. Zhuang, M. W. Lin, K. Xiao, R. G. Hennig, B. C. Sales, J. Q. Yan, and D. Mandrus, APL Mater. **3**, 041515 (2015).
[24] H. A. Bechtel, E. A. Muller, R. L. Olmon, M. C. Martin, and M. B. Raschke, Proc. Natl. Acad. Sci. USA **111**, 7191 (2014).
[25] E. A. Muller, B. Pollard, and M. B. Raschke, J. Phys. Chem. Lett. **6**, 1275 (2015).
[26] G. L. Carr, Rev. Sci. Instrum. **72**, 1613 (2001).
[27] O. Khatib, H. A. Bechtel, M. C. Martin, M. B. Raschke, and G. L. Carr, ACS Photon. **5**, 2773 (2018).
[28] S. Mastel, A. A. Govyadinov, C. Maissen, A. Chuvilin, A. Berger, and R. Hillenbrand, ACS Photon. **5**, 3372 (2018).
[29] B. Pollard, F. C. Maia, M. B. Raschke, and R. O. Freitas, Nano Lett. **16**, 55 (2016).
[30] J. Chen, M. Badioli, P. Alonso-González, S. Thongrattanasiri, F. Huth, J. Osmond, M. Spasenović, A. Centeno, A. Pesquera, P. Godignon, A. Zurutuza Elorza, N. Camara, F. J. G. de Abajo, R. Hillenbrand, and F. H. L. Koppens, Nature (London) **487**, 77 (2012).
[31] V. W. Brar, M. S. Jang, M. Sherrott, S. Kim, J. J. Lopez, L. B. Kim, M. Choi, and H. Atwater, Nano Lett. **14**, 3876 (2014).
[32] M. Liu, A. J. Sternbach, M. Wagner, T. V. Slusar, T. Kong, S. L. Bud'ko, S. Kittiwatanakul, M. M. Qazilbash, A. McLeod, Z. Fei, E. Abreu, J. Zhang, M. Goldflam, S. Dai, G. X. Ni, J. Lu, H. A. Bechtel, M. C. Martin, M. B. Raschke, R. D. Averitt, S. A.

Wolf, H. T. Kim, P. C. Canfield, and D. N. Basov, Phys. Rev. B **91**, 245155 (2015).
[33] X. Lu, O. Khatib, X. Du, J. Duan, W. Wei, X. Liu, H. A. Bechtel, F. D'Apuzzo, M. Yan, A. Buyanin, Q. Fu, J. Chen, M. Salmeron, J. Zeng, M. B. Raschke, P. Jiang, and X. Bao, Adv. Electron. Mater. **4**, 1700377 (2018).
[34] P. Kusch, N. Morquillas Azpiazu, N. S. Mueller, S. Mastel, J. I. Pascual, and R. Hillenbrand, J. Phys. Chem. C **122**, 16274 (2018).
[35] W. Klingen, R. Ott, and H. Hahn, J. Inorg. Gen. Chem. **396**, 271 (1973).
[36] K. Kurosawa, S. Saito, and Y. Yamaguchi, J. Phys. Soc. Jpn. **52**, 3919 (1983).
[37] E. Ressouche, M. Loire, V. Simonet, R. Ballou, A. Stunault, and A. Wildes, Phys. Rev. B **82**, 100408(R) (2010).
[38] P. A. Joy and S. Vasudevan, Phys. Rev. B **46**, 5134 (1992).
[39] P. A. Joy and S. Vasudevan, J. Phys. Chem. Solids **54**, 343 (1993).
[40] R. Kumar, R. N. Jenjeti, M. P. Austeria, and S. Sampath, J. Mater. Chem. C **7**, 324 (2019).
[41] C. T. Kuo, M. Neumann, K. Balamurugan, H. J. Park, S. Kang, H. W. Shiu, J. H. Kang, B. H. Hong, M. Han, T. W. Noh, and J. G. Park, Sci. Rep. **6**, 1 (2016).
[42] M. Hangyo, S. Nakashima, A. Mitsuishi, K. Kurosawa, and S. Saito, Solid State Commun. **65**, 419 (1988).
[43] M. Bernasconi, G. L. Marra, G. Benedek, L. Miglio, M. Jouanne, C. Julien, M. Scagliotti, and M. Balkanski, Phys. Rev. B **38**, 12089 (1988).
[44] D. B. Litvin, Acta Crystallogr. Sect. A **42**, 44 (1986).
[45] K. D. Hughey, A. J. Clune, M. O. Yokosuk, A. al-Wahish, K. R. O'Neal, S. Fan, N. Abhyankar, H. Xiang, Z. Li, J. Singleton, N. S. Dalal, and J. L. Musfeldt, Phys. Rev. B **96**, 180305(R) (2017).
[46] Q. Wang, Q. Zhang, X. Zhao, X. Luo, C. P. Y. Wong, J. Wang, D. Wan, T. Venkatesan, S. J. Pennycook, K. P. Loh, G. Eda, and A. T. Wee, Nano Lett. **18**, 6898 (2018).
[47] P. A. Joy and S. Vasudevan, J. Am. Chem. Soc. **114**, 7792 (1992).
[48] See Supplemental Material at http://link.aps.org/supplemental/10.1103/PhysRevB.100.075428 for traditional Raman and infrared spectra across the complete frequency window, with corresponding mode assignments. Also included is a discussion on signal-to-noise ratio in the near-field infrared response of atomically thin materials.
[49] G. Kresse and J. Furthmüller, Phys. Rev. B **54**, 11169 (1996).
[50] G. Kresse and D. Joubert, Phys. Rev. B **59**, 1758 (1999).
[51] J. P. Perdew, A. Ruzsinszky, G. I. Csonka, O. A. Vydrov, G. E. Scuseria, L. A. Constantin, X. Zhou, and K. Burke, Phys. Rev. Lett. **100**, 136406 (2008).
[52] S. L. Dudarev, G. A. Botton, S. Y. Savrasov, C. J. Humphreys, and A. P. Sutton, Phys. Rev. B **57**, 1505 (1998).
[53] A. Togo and I. Tanaka, Scr. Mater. **108**, 1 (2015).
[54] Y. Mathey, R. Clement, C. Sourisseau, and G. Lucazeau, Inorg. Chem. **19**, 2773 (1980).
[55] P. K. Jain, D. Ghosh, R. Baer, E. Rabani, and A. P. Alivisatos, Proc. Natl. Acad. Sci. USA **109**, 8016 (2012).
[56] E. Pensa, E. Cortés, G. Corthey, P. Carro, C. Vericat, M. H. Fonticelli, G. Benítez, A. A. Rubert, and R. C. Salvarezza, Acc. Chem. Res. **45**, 1183 (2012).
[57] X.-M. Zhao, H.-y. Liu, A. F. Goncharov, Z.-W. Zhao, V. V. Struzhkin, H.-K. Mao, A. G. Gavriliuk, and X.-J. Chen, Phys. Rev. B **99**, 024111 (2019).
[58] J. Ribeiro-Soares, R. M. Almeida, E. B. Barros, P. T. Araujo, M. S. Dresselhaus, L. G. Cançado, and A. Jorio, Phys. Rev. B **90**, 115438 (2014).
[59] H. S. Kim and H. Y. Kee, Phys. Rev. B **93**, 155143 (2016).
[60] S.-Y. Park, S.-H. Do, K.-Y. Choi, D. Jang, T.-H. Jang, J. Schefer, C.-M. Wu, J. S. Gardner, J. M. S. Park, J.-H. Park, and S. Ji, arXiv:1609.05690.
[61] S.-H. Do, S.-Y. Park, J. Yoshitake, J. Nasu, Y. Motome, Y. S. Kwon, D. Adroja, D. Voneshen, K. Kim, T.-H. Jang, J.-H. Park, and K.-Y. Choi, Nat. Phys. **13**, 1079 (2017).